Journal of Materials Chemistry A

ROYAL SOCIETY OF CHEMISTRY

PAPER

View Article Online
View Journal | View Issue

Cite this: *J. Mater. Chem. A*, 2026, **14**, 8836

Iodine-driven artificial SEI layer for high performance lithium metal batteries in an SO_2-based electrolyte

Jiwhan Lee, Seung Do Mun, Seong Hoon Choi and Hansu Kim *

Received 11th October 2025
Accepted 13th January 2026

DOI: 10.1039/d5ta08305b

rsc.li/materials-a

Lithium metal anodes offer high theoretical capacity with a low redox potential; however, an unstable solid electrolyte interphase (SEI), lithium dendrite formation, and limited cycling performance limit their practical applications. While SO_2-based inorganic electrolytes provide high ionic conductivity and inherent nonflammability, their high reactivity with lithium forms thick and unstable SEI layers that are primarily composed of LiCl and lithium–sulfur–oxy compounds. In this study, we demonstrate an SEI engineering strategy using a molecular iodine (I_2)-containing $LiAlCl_4$–$3SO_2$ electrolyte to control the composition of the SEI formed at the interface of the lithium metal electrode. The I_2 acts as a redox mediator that promotes the formation of Li_2S and Li_2O-enriched artificial SEI layers in lithium metal, replacing the typical LiCl-dominant interfacial film. This Li_2S/Li_2O-rich artificial SEI exhibited enhanced Li^+ transport properties and mechanical stability compared to the native SEI, thereby suppressing lithium dendrite formation and mitigating parasitic reactions during cycling. The electrochemical evaluation demonstrated improved cycling stability in both Li//Li symmetric cells and Li//$LiFePO_4$ full cells across various current densities.

1 Introduction

The growing demand for energy storage systems with high energy density for electric vehicles and grid-scale applications has driven the development of advanced lithium-ion battery systems.[1–4] The lithium metal anode is considered the most promising next-generation lithium storage material because of its high theoretical capacity (~3860 mA h g^{-1}) and low redox potential (−3.04 V *vs.* SHE).[5–7] However, the practical implementation of lithium metal anodes remains hindered by several challenges, including interfacial instability, low coulombic efficiency, uncontrolled lithium dendrite growth, and continuous side reactions during cycling.[5,8–10] Extensive efforts have been made to improve interfacial stability by modifying electrolyte formulations to control the interfacial reactions of lithium metal with the electrolyte,[11–13] modifying the surface of the lithium metal anode,[14–16] and engineering robust artificial solid electrolyte interphase (SEI) layers[17–20] to regulate the lithium deposition behavior. Recently, additive-assisted artificial SEI engineering has also attracted growing attention as an effective strategy to regulate Li^+ flux, homogenize interfacial reactions, and suppress dendrite formation. For instance, Wang *et al.* demonstrated that additive-derived inorganic species incorporated into SEI layers can significantly enhance ionic conductivity and mechanical stability, leading to improved lithium deposition uniformity.[21] Moreover, the controlled interfacial chemistry combined with three-dimensional lithiophilic host structures enables confined and homogeneous lithium deposition even at high areal capacities.[22] In addition, the construction of artificial inorganic/organic composite SEI layers using functional additives has been reported to simultaneously enhance the ionic conductivity, interfacial robustness, and electrochemical reversibility of lithium metal anodes, enabling stable cycling even under high-voltage conditions.[23] These recent studies highlight the critical role of additive-driven artificial SEI design in controlling lithium deposition behavior and stabilizing lithium metal anodes. Although most of these efforts have focused on organic electrolyte systems, they still suffer from volatility, flammability, and limited long-term stability. Recent attention has shifted toward non-organic electrolytes with intrinsic nonflammability.[2,24–28] Among alternative electrolyte systems, nonflammable SO_2-based liquid electrolytes, such as $LiAlCl_4$–$3SO_2$ (Li–SO_2), offer significant benefits including nonflammability and high ionic conductivity (~100 mS cm^{-1}).[29] However, Li–SO_2 liquid electrolytes are highly reactive to lithium metal, leading to the formation of thick and unstable SEI layers mainly composed of LiCl and lithium–sulfur–oxide compounds.[30–37] Li_2S and Li_2O are beneficial for lithium metal anodes because of their contribution to the electrochemical and mechanical stability of the SEI layer.[38–40] Li_2S is an ion-conductive sulfide compound that facilitates lithium-ion transport through the SEI,[41–43] while Li_2O is a mechanically rigid compound that helps maintain the

Department of Energy Engineering, Hanyang University, 222 Wangsimni-ro, Seongdong-gu, Seoul, 04763, Republic of Korea. E-mail: khansu@hanyang.ac.kr

structural integrity of the interphase during cycling.[44–46] However, despite these benefits, the lithium metal electrode in Li–SO_2 electrolyte suffers from unstable cycling behavior and continuous side reactions with the electrolyte. This suggests that the amount of Li_2S and Li_2O formed in the SEI of the lithium electrode might be insufficient to effectively suppress dendritic growth or maintain SEI integrity over prolonged cycling. Therefore, augmenting the formation of Li_2S and Li_2O in the SEI of the lithium electrode may be essential for improving the interfacial stability of lithium metal anodes using Li–SO_2 electrolytes. In this study, we demonstrate an interfacial engineering strategy that utilizes lithium iodide as an additive for lithium metal anodes with Li–SO_2 electrolyte, enabling the *in situ* generation of molecular iodine (I_2) *via* a spontaneous redox disproportionation reaction.[47–51] When lithium metal electrodes are pretreated by controlled immersion in this I_2-containing Li–SO_2 electrolyte (I_2–Li–SO_2), I_2 acts as a catalytic mediator to facilitate the preferential formation of the Li_2S and Li_2O-enriched SEI *via* I_2/I^- redox transformation.[48,49] While a highly rough native SEI was formed in pristine Li–SO_2 electrolyte, mainly composed of LiCl with limited ion-conductive components, the engineered interphase was relatively uniform and compact, thus showing significantly enhanced electrochemical stability. The resulting protective layer effectively mitigates lithium dendrite formation and suppresses parasitic side reactions to enable uniform lithium deposition and improve long-term cycling performance. This approach provides a practical strategy for stabilizing lithium metal electrodes in the Li–SO_2 electrolyte system and advances high-performance lithium metal battery technologies.

2 Experimental section

2.1 Electrolyte synthesis

The pristine $LiAlCl_4$–$3SO_2$ electrolyte was prepared by mixing the same molar amounts of LiCl and $AlCl_3$ powder in a sealed bottle, followed by blowing SO_2 gas with stirring to promote the chemical reaction between the SO_2 gas and the powder mixture. After the completion of the reaction, the resulting electrolyte was transferred to an Ar-filled glovebox to prevent moisture exposure. For the preparation of iodine-containing electrolytes, LiI, LiCl, and $AlCl_3$ powders were mixed at a molar ratio of 0.1 : 0.9 : 1, respectively, during the initial powder-mixing stage, enabling *in situ* I_2 formation within the electrolyte system. The subsequent synthesis procedure was identical to that of the pristine electrolyte, including SO_2 gas introduction, reaction completion, and collection under inert atmospheric conditions. For the concentration-dependent study, the LiI fraction was further varied while keeping the total salt content constant, using LiI : LiCl : $AlCl_3$ molar ratios of 0.05 : 0.95 : 1 and 0.20 : 0.80 : 1, and the same SO_2 introduction and handling procedures were applied.

2.2 Electrochemical measurements

CR2032 coin-type symmetric Li//Li cells were assembled using 200 μm-thick and 18 μm-thick lithium metal (Honjo metal, Japan), glass fiber filter separators (GC50, Advantec), and an SO_2-based electrolyte in an Ar-filled glovebox. $LiFePO_4$ (LFP) cathodes were prepared by hand-mixing using an agate mortar, combining 80 wt% active material (LFP; China), 10 wt% conductive agent (Super-P, TIMCAL, Switzerland), and 10 wt% polyvinyl fluoride binder (KF1100, Kureha Chemical Industry Co., Ltd, Japan) dissolved in *N*-methyl-2-pyrrolidinone (99.9 wt%, Sigma Aldrich, USA). The resulting slurry was cast onto aluminium foil using a Baker film applicator, vacuum-dried overnight at 200 °C, and compressed at 200 kg cm^{-2}. Both Li//Li symmetric cells and Li//LFP full cells were assembled in an Ar-filled glovebox and left for 12 h at 25 °C before electrochemical evaluation using a TOSCAT battery testing system. For Li//LFP full-cell testing, two types of $LiFePO_4$ cathodes were employed: areal loadings of 12 mg cm^{-2} for 0.5C and 9 mg cm^{-2} for 2C current density evaluation, corresponding to areal capacities of 2 mA h cm^{-2} and 1.5 mA h cm^{-2}, respectively. After calendering, the electrode densities were ~2.3 g cc^{-1} (12 mg cm^{-2}) and ~2.2 g cc^{-1} (9 mg cm^{-2}). The cells were subjected to galvanostatic charge–discharge cycling to evaluate the electrochemical performance of pristine and I_2-modified lithium anodes paired with LFP cathodes. CV and LSV tests of the electrolytes were performed using a potentiostat (VSP-300, BioLogic) in a three-electrode beaker-type cell (with glassy carbon as the working electrode and Li-metal foil as the counter and reference electrodes) at a scan rate of 0.1 mV s^{-1} with a voltage window of 0.005–4.5 V for CV tests and 0.005–5 V for LSV tests.

2.3 Electrochemical characterization

Raman spectra of the electrolytes were acquired using a Raman spectrometer (DXR3xi, Thermo Fisher Scientific) to analyze the molecular structure and composition of SO_2-based electrolytes. EIS was performed using an impedance-analyzing potentiostat (VSP-300, BioLogic) with an AC amplitude of 10 mV over a frequency range of 1 mHz to 1 MHz to evaluate interfacial resistance characteristics. The surface morphology and cross-sectional structures of lithium metal electrodes before and after cycling in $LiAlCl_4$–$3SO_2$ electrolytes were examined using field-emission SEM (FE-SEM; JEOL JSM-7000F). For detailed microstructural analysis, focused ion beam FE-SEM (Helios) was employed. Cross-sectional TEM analysis was performed using a transmission electron microscope (JEM-2010, JEOL). XPS (Thermo Fisher Scientific) was used to analyze the surface chemical composition and oxidation states of lithium metal electrodes after electrochemical cycling. All XPS profiles were calibrated by aligning the C 1s peak to 284.8 eV to ensure consistent binding energy referencing.

3 Results and discussion

3.1 Formation and characterization of the Li_2S/Li_2O-enriched artificial SEI layer

Fig. 1 presents a comprehensive overview of the interfacial engineering strategy for lithium metal electrodes using I_2-containing $LiAlCl_4$–$3SO_2$ systems (I_2–Li–SO_2). The electrolyte was

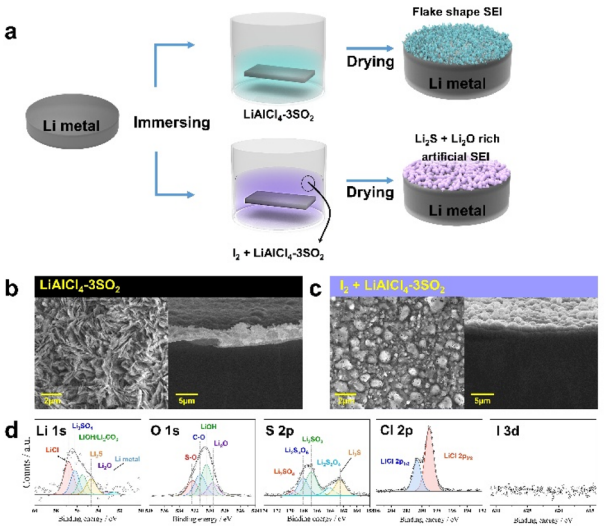

Fig. 1 Artificial Li_2S/Li_2O-rich SEI formation *via* I_2-modified $LiAlCl_4$–$3SO_2$ electrolyte. (a) Schematic of lithium metal surface modification using $LiAlCl_4$–$3SO_2$ and I_2-containing $LiAlCl_4$–$3SO_2$. Surface and cross-sectional SEM images of modified lithium electrodes immersed in (b) $LiAlCl_4$–$3SO_2$ and (c) I_2-containing $LiAlCl_4$–$3SO_2$. (d) XPS profiles showing the Li 1s, O 1s, S 2p, Cl 2p, and I 3d regions of the lithium metal surface after treatment with I_2-containing $LiAlCl_4$–$3SO_2$.

prepared by dissolving LiCl, $AlCl_3$, and LiI with SO_2 gas, followed by the spontaneous formation of liquid electrolyte with I_2, showing a color change to deep purple (Fig. S1). This color change originates from the disproportionation reaction of iodide ions and the successful generation of I_2 species in the electrolyte. Raman spectroscopy (Fig. S2) revealed characteristic peaks at 209, 417, and 627 cm^{-1} corresponding to I_2 vibrations in the I_2–Li–SO_2 system.[52] We further examined the LiI concentration dependency (in the 0.05–0.20 M range, compared to that of LiCl in the first synthesis process) on the performance of the iodine-containing $LiAlCl_4$–$3SO_2$ electrolyte. Fig. S3 shows that the 0.05 M LiI electrolyte exhibits a lighter color and weaker normalized I_2-related Raman intensity as well, whereas the 0.10 and 0.20 M electrolytes show similar dark coloration with nearly identical Raman features. Based on these results, the 0.10 M condition was selected as the representative I_2-modified electrolyte for electrochemical characterization, and its redox behavior and electrochemical stability were further examined by cyclic voltammetry (CV) and linear sweep voltammetry (LSV) (Fig. S4). The I_2-containing electrolyte shows a narrower electrochemical stability window than the pristine $LiAlCl_4$–$3SO_2$ electrolyte.[48,53,54] The decrease in the electrochemical window of I_2–Li–SO_2 electrolyte owing to electrochemical reduction of I_2 at approximately 3.7 V (*vs.* Li/Li^+) suggests that the I_2-containing Li–SO_2 electrolyte is insufficient for lithium rechargeable batteries. Despite this electrochemical limitation, the I_2–Li–SO_2 system can be used for the surface modification of lithium metal anodes. Fig. 1a shows a schematic of the surface modification process by immersing lithium metal into unmodified Li–SO_2 and I_2–Li–SO_2 electrolytes (Fig. S5). Fig. 1b and c show the top-view and cross-sectional scanning electron microscopy (SEM) images of the Li metal after immersion in the pristine and I_2-containing electrolytes for 24 h, respectively. Fig. 1b shows the formation of a native SEI layer with an irregular, flake-type morphology of lithium metal after immersion in Li–SO_2 electrolyte for 24 h. Fig. 1c shows a uniform SEI layer with a round morphology after dipping in the I_2–Li–SO_2 electrolyte, which is mainly composed of spherical particles forming a conformal layer with thickness of approximately 2 μm. SEM observation shows that at the electrolyte with 0.10 M LiI, Li metal has the most uniform rounded/conformal surface layer, whereas dipping of Li metal in the 0.05 and 0.20 M electrolytes led to denser film-like layers with different thicknesses (Fig. S6). X-ray photoelectron spectroscopy (XPS) was employed to obtain insights into the chemical composition and interfacial chemistry of the lithium metal surfaces after the immersion process. Fig. 1d shows the XPS profiles of lithium metal after immersion in the I_2–Li–SO_2 electrolyte (I_2-modified lithium). The Li 1s spectrum shows distinct peaks at 54.5 eV (ref. 55) and 53.5 eV,[56] corresponding to Li_2S and Li_2O, respectively. We further compared the surface SEI chemistry after iodine treatment at different LiI levels (0.05 and 0.20 M) by XPS analysis of the Li 1s, O 1s, S 2p, Cl 2p, and I 3d regions (Fig. S7). XPS spectra after dipping (Fig. S7) show that the chemical compositions of the SEIs formed by dipping Li metal in the electrolytes are almost the same. All of this indicates significantly higher surface concentrations of these inorganic compounds compared to lithium metal immersed in pristine Li–SO_2 electrolyte (Fig. S8). The O 1s and S 2p spectra of lithium metal after immersion in the I_2–Li–SO_2 electrolyte further confirm this observation, showing distinct Li_2O and Li_2S peaks at 528.8 and 162.5 eV, respectively. In contrast, the Li 1s spectrum of lithium metal immersed in pristine Li–SO_2 electrolyte shows a peak at 56.2 eV for LiCl.[57] The O 1s and S 2p spectra are dominated by peaks corresponding to the Li–S–O compound, with only minor contributions from Li_2O and Li_2S. This comparison reveals that the introduction of I_2 into the Li–SO_2 electrolyte alters the reaction chemistry of lithium metal with the SO_2-based electrolyte, leading to changes in the main SEI species on the surface of the lithium metal through the following reactions:[49]

$$2I^- + SO_2 + 6Li \rightarrow Li_2S + 2Li_2O + I_2 \quad (1)$$

$$Li_2SO_4 + I_2 + 8Li \rightarrow Li_2S + 4Li_2O + 2I^- \quad (2)$$

I_2 in the electrolyte acts as a chemical mediator, promoting the formation of SEI components such as Li_2O and Li_2S, which are expected to enhance the interfacial stability of the lithium metal electrode. To verify this I_2-mediated chemistry, *ex situ* Raman spectra were collected for the I_2–Li–SO_2 electrolyte before and after lithium dipping (Fig. S9), together with XPS analysis of lithium subjected to sequential treatment (pristine Li–SO_2 dipping followed by I_2–Li–SO_2 dipping) as shown in Fig. S10. After dipping, the Raman bands for $AlCl_4^-$ decrease in intensity, indicating the interfacial reaction between lithium and the electrolyte, whereas the characteristic I_2 band remains essentially unchanged (Fig. S9).[58] Notably, the Raman band near

~170 cm^{-1} decreases after lithium dipping, suggesting a change in the iodine species associated with weak iodine–iodide interactions.[52,59] This observation is consistent with reversible I_2/I^- interfacial mediation during the dipping process, rather than irreversible consumption of iodine. Consistently, the absence of a detectable I 3d signal was observed in the XPS spectra (Fig. 1d), confirming that iodine was not incorporated as a SEI component. It should be noted that the XPS spectra of Li metal after the sequential treatment show that I_2 can transform a pre-formed SEI to a Li_2S/Li_2O-rich composition without iodine incorporation, supporting that I_2 acts as a catalytic mediator rather than a consumable additive (Fig. S10).

3.2 Lithium deposition behavior on I_2-modified electrodes

Fig. 2 shows top-view SEM images of lithium deposits formed on the lithium metal electrode, obtained after three cycles using pristine lithium and the I_2-modified lithium with Li–SO_2 electrolyte at various current densities and areal capacities. These images offer critical insights into how surface pretreatment affects the morphology of lithium deposits under various electrochemical conditions (0.5–3 mA cm^{-2} for current density and 1–5 mA h cm^{-2} for areal capacity). In the pristine lithium electrode (Fig. 2a), lithium deposits appear relatively flat and uniform under mild conditions, such as 0.5 mA cm^{-2} and 1 mA h cm^{-2}. However, as the current density and areal capacity increased, the lithium metal surface became rough, with lithium filament growth. This dendritic morphology results from the uneven Li^+ flux and high interfacial reactivity of lithium metal with the Li–SO_2 electrolyte. In contrast, the I_2-modified lithium electrode (Fig. 2b) shows rounded and compact deposits under all conditions. Even at high current densities, the I_2-modified lithium maintained a relatively smooth surface without needle-shaped deposits, while a floc-like overlayer was formed. SEM-EDS mapping (Fig. S11) indicates that this overlayer shows stronger O, S, Cl, and Al signals compared to the surface features formed on pristine lithium. This suggests that the pre-formed artificial SEI was partially preserved during cycling and continued to function as a protective scaffold that guides more uniform Li deposition and suppresses dendritic growth under harsh conditions. This comparison suggests that the Li_2S and Li_2O-enriched SEI layer effectively controlled lithium nucleation and growth in the Li–SO_2 electrolyte system, thereby maintaining uniform lithium-ion flux and preventing high-surface-area dendrite formation. This uniform and rounded lithium deposition behavior indicates that ion transport in the I_2-modified SEI is dominated by fast lateral Li^+ diffusion along the SEI/Li interface rather than vertical Li penetration.[60,61] The Li_2S/Li_2O-rich inorganic interphase with abundant grain boundaries provides rapid interfacial diffusion pathways, which effectively homogenize the surface Li-ion flux and suppress the localized current amplification responsible for dendritic growth.[62]

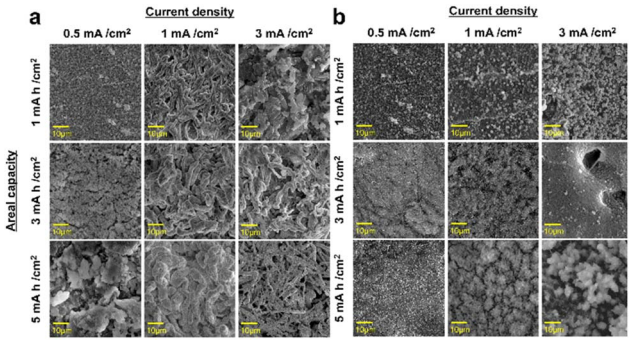

Fig. 2 Effect of current density and areal capacity on Li deposition morphology. FIB-SEM images of the Li deposit for (a) the pristine lithium metal electrode and (b) I_2-modified Li-metal electrode in a $LiAlCl_4$–$3SO_2$ inorganic electrolyte after three cycles under various areal capacity and current density conditions.

3.3 Electrochemical performance of I_2-modified lithium electrodes

Fig. 3 shows that the lithium symmetric cells with an artificial SEI layer on the lithium metal anode exhibited stable operation for over 1000 cycles at current densities of 1 and 3 mA cm^{-2}, with a fixed areal capacity of 3 mA h cm^{-2} with the Li–SO_2 electrolyte. At a current density of 1 mA cm^{-2} (Fig. 3a), the pristine lithium electrode exhibited a slightly lower average overpotential than the modified electrode, but showed potential fluctuations between 2400 and 3600 h (corresponding to 400–600 cycles), which originated from non-uniform lithium deposition and an unstable SEI layer on the surface of the pristine lithium electrode (Fig. S12). In contrast, the I_2-modified electrode maintains stable electrochemical deposition and

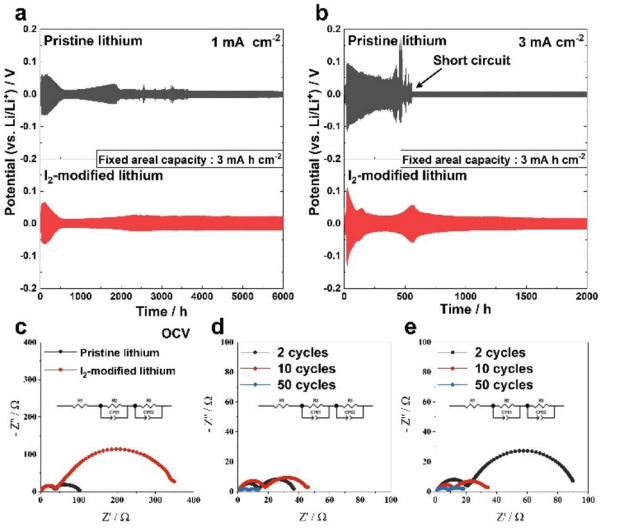

Fig. 3 Electrochemical performance and interfacial resistance of pristine and I_2-modified lithium electrodes, and electrochemical performance of Li//Li symmetric cells with pristine and I_2-modified lithium electrodes. Cycling behavior at current densities of (a) 1 mA cm^{-2} and (b) 3 mA cm^{-2} with a fixed areal capacity of 3 mA h cm^{-2}. (c) EIS analysis after 12 h at open-circuit voltage. Nyquist plots after 2, 10, and 50 cycles for (d) pristine lithium and (e) I_2-modified lithium electrodes.

stripping of lithium metal without abrupt changes in the overpotential for over 6000 h (2000 cycles). In particular, voltage profiles enlarged near 5000 h (Fig. S13) clearly show that the I_2-modified Li//Li cell retains periodic plating/stripping oscillations without a short-circuit-like flat response, indicating that the slight long-term potential evolution arises from gradual interfacial reorganization and mass-transport polarization rather than catastrophic failure.[63–66] Although the modified electrode exhibited a slightly higher overpotential compared with pristine lithium, the Li_2S and Li_2O-enriched SEI effectively suppressed parasitic reactions and enabled uniform lithium deposition. At the higher current density of 3 mA cm^{-2} and areal capacity of 3 mA h cm^{-2} (Fig. 3b), the performance difference becomes more pronounced. The pristine lithium electrode showed a sharp increase in overpotential after 200 h (corresponding to 100 cycles) with voltage fluctuations, followed by a short-circuit failure at 562 h (281 cycles) (see the enlarged profile in Fig. S14). Such degradation of the pristine lithium electrode is attributed to the accelerated SEI breakdown and aggressive dendrite growth under high current conditions. In contrast, the I_2-modified lithium electrode demonstrates stable charge–discharge behavior for over 2000 h (1000 cycles), indicating that the modified SEI layer effectively withstood high current conditions and suppressed dendrite formation during extended cycling. Note that the electrolyte with 0.10 M LiI showed the most favorable overall performance among the investigated formulations (Fig. S15). To further evaluate interfacial stability, Li//Li symmetric cell tests were conducted at both low (1 mA h cm^{-2}) and high (5 mA h cm^{-2}) areal capacities as shown in Fig. S16. The I_2-modified lithium maintained stable cycling behavior even at high areal capacity, whereas pristine lithium suffered from early short-circuit failure. Moreover, under 18 μm thin-lithium conditions, the I_2-modified lithium electrode exhibited a uniform and dense interfacial structure as revealed by cross-sectional SEM analysis (Fig. S17), and demonstrated stable and reversible plating/stripping behavior in the corresponding electrochemical test (Fig. S18), confirming the strong protective capability of the artificial SEI. In addition, to identify the current density limitation of the I_2-modified lithium electrode, Li symmetric cell rate tests were performed from 0.1 to 10 mA cm^{-2} at a fixed areal capacity of 1 mA h cm^{-2}. The I_2-modified lithium maintained stable operation across the entire current range, indicating that the artificial SEI effectively accommodates fast Li^+ transport over a wide kinetic regime (Fig. S19).[67]

This remarkable improvement in stability also highlights the role of the artificial SEI layer in enabling the reliable operation of lithium metal electrodes. Because the cycling stability of lithium electrodes is closely related to the interfacial resistance, electrochemical impedance spectroscopy (EIS) (Fig. 3c–e) at different cycles was employed to analyze the resistance of the naturally formed SEI and preformed Li_2S/Li_2O artificial SEI on the lithium metal electrode. As shown in Fig. 3c, the SEI resistance (R_{sei}) of the I_2-modified lithium before testing was higher than that of pristine lithium, indicating that the artificial SEI layer already formed on the electrode surface prior to cycling (Table S1). This preformed layer, while increasing the initial impedance, may provide a more compact and denser interface with the electrolyte compared to that of the pristine lithium electrode. Fig. 3d shows the EIS profiles of the pristine lithium metal electrodes after 2, 10, and 50 cycles. After 10 cycles, the pristine lithium electrode showed an increase in R_{sei}, possibly due to the thickening of the SEI caused by side reactions between the lithium and electrolyte during cycling. However, after 50 cycles, a sharp decrease in R_{sei} was observed, which can be attributed to SEI breakdown and surface structural changes during repeated cycling (Table S2).[68] In contrast, the EIS spectra of the I_2-modified lithium metal electrode exhibited a different behavior compared to those of the pristine lithium electrode, as shown in Fig. 3e. Although the initial R_{sei} was higher than that of pristine lithium, the resistance of the SEI layer for the I_2-modified lithium electrode gradually decreased with cycling. This suggests that the Li_2S/Li_2O-rich artificial SEI enabled highly stable lithium deposition and stripping over extended cycles.[69] Overall, the I_2-modified lithium shows a higher initial SEI resistance and charge-transfer resistance due to the presence of the preformed inorganic layer, and both resistances gradually decrease with cycling and become comparable to those of pristine lithium. The exchange current density of the Li electrode is well known to reflect the electrochemical kinetics for the Li deposition/dissolution reaction according to the complete overpotential–current relationship.[70] Since R_{ct} is inversely related to effective charge-transfer kinetics under an identical symmetric cell, the reduction of R_{ct} for the I_2-modified electrode indicates that the artificial SEI does not hinder, and may even facilitate the effective interfacial exchange kinetics during cycling.

Fig. 4 shows cross-sectional SEM images of lithium metal electrodes obtained from cycled Li//Li symmetric cells with the Li–SO_2 electrolyte after 2, 20, and 50 cycles at a current density of 3 mA cm^{-2} and an areal capacity of 3 mA h cm^{-2}. The pristine lithium electrodes showed severe morphological degradation

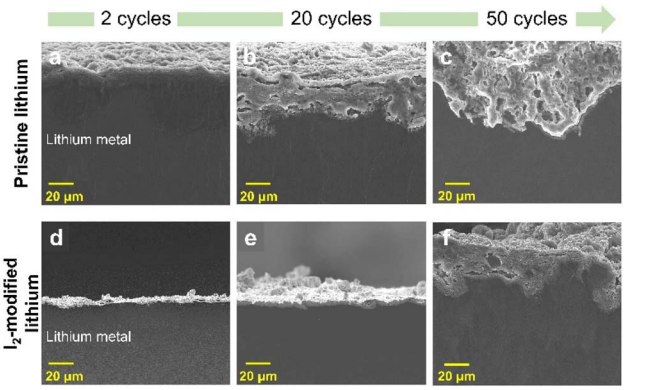

Fig. 4 Cross-sectional SEM analysis of SEI evolution during cycling, and cross-sectional SEM analysis of lithium metal electrodes after symmetric cell cycling. (a–c) Pristine lithium electrode after cycling at a current density of 3 mA cm^{-2} with areal capacity of 3 mA h cm^{-2} for 2, 20, and 50 cycles, respectively. (d–f) I_2-modified lithium electrode after cycling under identical conditions, demonstrating the formation of dense, uniform SEI layers.

over extended cycling (Fig. 4a–c and S20a). The thickness of the porous surface layer dramatically increased from ~7 μm after 2 cycles to ~30 μm after 20 cycles, ultimately reaching 100–180 μm after 50 cycles. This progressive thickening indicates continuous parasitic reactions between the lithium metal and electrolyte, leading to the formation of highly porous lithium deposits. In contrast, I_2-modified lithium electrodes maintained a relatively stable morphology even after 50 cycles, with the interfacial layer thickness remaining below ~20 μm (Fig. 4d–f and S20b). The surface layer, consisting of both SEI components and lithium deposits, remained thin and dense. This compact interfacial layer maintained on the I_2-modified lithium electrode indicates that Li transport is dominated by fast lateral interfacial diffusion rather than vertical Li penetration, which is mechanically suppressed by the rigid inorganic Li_2S/Li_2O framework.[71,72] Such morphological and dimensional stability of the electrode is well maintained, effectively suppressing continuous parasitic reactions with the electrolyte and leading to enhanced long-term cycling stability.

Fig. 5 and 6 show the XPS profiles of lithium metal electrodes from the Li//Li symmetric cells after various cycles. For the pristine lithium electrodes (Fig. 5), the Li 1s spectra were dominated by the peak at 56.2 eV, corresponding to LiCl, which progressively accumulates and remains as the main SEI component throughout cycling. Very small peaks for Li_2S (54.5 eV) and Li_2O (53.4 eV) were observed, indicating the limited formation of beneficial inorganic species in the SEI of the pristine lithium electrode. The O 1s spectra of the pristine lithium electrode showed that S–O and C–O compounds were the major components of the SEI layer, while the Li_2O observed at 528.8 eV remained weakly visible throughout the cycling. The S 2p spectra showed the progressive increase of the peaks for the Li–S–O compound with cycling, while the Li_2S signal at 162.5 eV remained consistently weak. These results indicate that the SEI of pristine lithium mainly consisted of LiCl, with Li_2S and Li_2O as minor constituents. In contrast, the XPS profiles of the I_2-modified lithium electrode (Fig. 6) showed that the composition of the SEI was modified by introducing iodine.

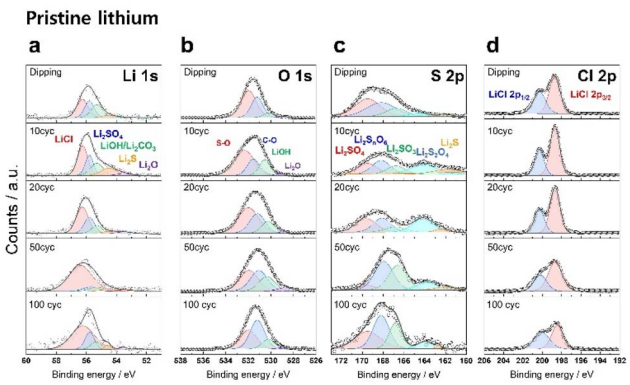

Fig. 5 XPS spectra evolution of pristine lithium metal during cycling. XPS analysis of the surface layer of the pristine lithium metal for (a) Li 1s, (b) O 1s, (c) S 2p, and (d) Cl 2p after dipping, 10 cycles, 20 cycles, 50 cycles, and 100 cycles using $LiAlCl_4$–$3SO_2$.

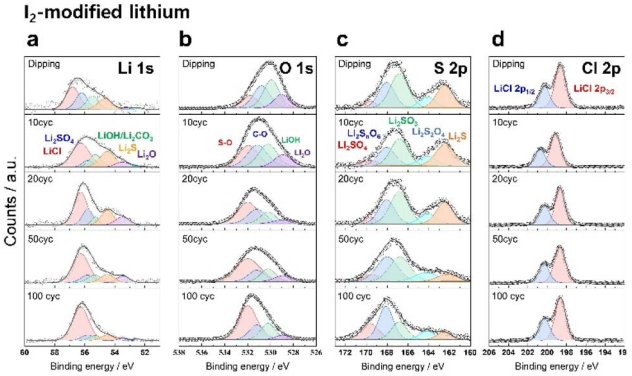

Fig. 6 XPS spectra evolution of I_2-modified lithium metal during cycling. XPS analysis of the surface layer of the I_2-modified lithium metal electrode for (a) Li 1s, (b) O 1s, (c) S 2p, and (d) Cl 2p after dipping, 10 cycles, 20 cycles, 50 cycles, and 100 cycles using $LiAlCl_4$–$3SO_2$.

The Li 1s spectra revealed strong peaks for Li_2S (54.5 eV) and Li_2O (53.5 eV), which remained prominent even after 50 cycles together with LiCl (56.2 eV). However, with continued cycling, the intensity of the LiCl peak progressively increased, suggesting the gradual development of LiCl-containing outer layers on the initially formed Li_2S/Li_2O-based layer. This configuration was further supported by the O 1s and S 2p spectra, which revealed the enrichment of Li_2S and Li_2O in the modified SEI layer of the I_2-modified lithium metal electrode. Notably, the O 1s spectra showed that the intensity of the peaks for the S–O and Li–S–O species became more pronounced during cycling, while the Li_2O peak remained consistently detectable. The S 2p spectra indicated an increase in Li–S–O species with the presence of Li_2S. The Cl 2p spectra showed only LiCl peaks, with no additional byproducts. These findings indicate that there were two layers in the SEI layer of the I_2-modified lithium electrode. The Li_2S/Li_2O-rich inner layer remained structurally intact throughout cycling, while the outer layer, mainly composed of LiCl and Li–S–O compounds, showed a gradual increase in thickness during cycling. The cross-sectional TEM (Fig. S21)[73,74] and depth-profiling XPS collected at different cycle numbers (Fig. S22) further support the proposed bilayer structure, revealing a dense and continuous SEI containing Li_2O/Li_2S domains. The depth-resolved XPS confirms that Li_2S/Li_2O components remain detectable up to 100 cycles, indicating a persistent inorganic-rich inner framework. This structural feature of the SEI was consistent with the EIS fitting results (Table S2). Although the pre-formed inorganic SEI initially increases interfacial resistances, both R_{sei} and R_{ct} progressively decrease and then stabilize upon cycling, indicating that the interphase becomes progressively more ion-conductive and kinetically stable while retaining its robust inorganic framework rather than undergoing SEI breakdown. Such a preformed layer can accommodate repeated interfacial cycling, thereby sustaining stable electrochemical performance. In contrast, the pristine lithium electrode develops a thick and mechanically fragile SEI.

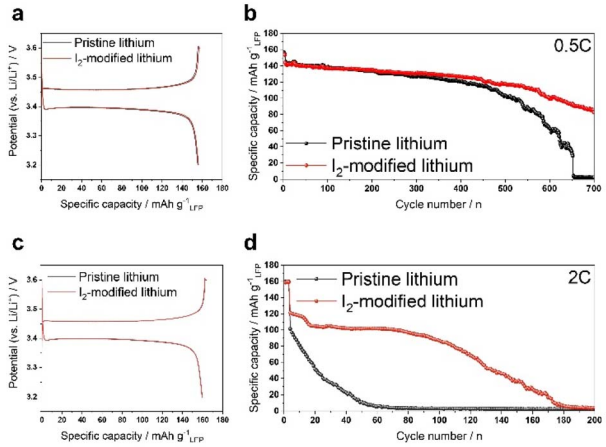

Fig. 7 Electrochemical performance of pristine and I_2-modified lithium metal anodes with $LiFePO_4$ cathodes, and electrochemical performance of $LiFePO_4$ cathodes with pristine and I_2-modified lithium metal anodes in $LiAlCl_4$–$3SO_2$ electrolyte. (a) The initial galvanostatic charge–discharge voltage profiles and (b) cycling performance at 0.5C (1 mA cm^{-2}) with an areal capacity of 2 mA h cm^{-2}. (c) Initial voltage profiles and (d) cycling performance at 2C (3 mA cm^{-2}) with an areal capacity of 1.5 mA h cm^{-2}.

To validate the practical applicability of the I_2-modified lithium metal anodes, the full-cell performance was evaluated using $LiFePO_4$ (LFP) cathodes in Li–SO_2 electrolyte systems. Fig. 7 presents a comparison of the electrochemical performance of the pristine and I_2-modified lithium anodes paired with LFP cathodes under different current density conditions. At a current density of 1 mA cm^{-2}, both electrodes exhibited initial coulombic efficiencies exceeding 99.3% (Fig. 7a). However, the long-term cycling performance (Fig. 7b) reveals distinct differences in stability. The I_2-modified lithium anode maintains a superior capacity retention of 63.9% after 600 cycles, while the pristine lithium anode shows only 39.7% of its initial capacity after the same number of cycles, which can be attributed to the physicochemical properties of the SEI layer of each lithium electrode. At a higher current density of 3 mA cm^{-2}, both systems demonstrated comparable initial coulombic efficiencies of over 96.9% (Fig. 7c). However, the I_2-modified anode demonstrated superior high-rate performance, maintaining better capacity retention throughout the extended cycling (Fig. 7d). These results confirm that the artificial SEI not only stabilizes the interface but also facilitates lithium-ion transport, supporting high-rate battery operation.

4 Conclusions

We demonstrated that a Li_2S and Li_2O-enriched artificial SEI layer, pre-formed by dipping a metal electrode in an I_2-containing $LiAlCl_4$–$3SO_2$ electrolyte, effectively suppressed dendritic lithium growth and mitigated side reactions between the lithium metal and electrolyte. This inorganic interphase exhibited high chemical and electrochemical stability during repeated cycling without continuous side reactions. Symmetric lithium cells with the modified electrode achieved long-term cycling stability over 1000 cycles even under high current densities. Li//LFP full cells demonstrated significantly improved capacity retention of 63.9% after 600 cycles. These results show that forming a stable Li_2S/Li_2O-enriched artificial SEI through an I_2-containing $LiAlCl_4$–$3SO_2$ pretreatment is an effective route to improve the durability of lithium metal anodes in SO_2-based electrolyte systems. While the present study validates the effectiveness of iodine-mediated interfacial stabilization in coin-type cells, translating SO_2-based inorganic electrolytes to pouch-cell formats remains challenging due to SO_2 gas evolution during the sealing process.

Author contributions

Jiwhan Lee: conceptualization, data curation, formal analysis, investigation, visualization, methodology, writing – original draft, writing – review & editing. Seung Do Mun: conceptualization, formal analysis, investigation, methodology. Seong Hoon Choi: conceptualization, investigation. Hansu Kim: writing – original draft, writing – review & editing, project administration, supervision.

Conflicts of interest

There are no conflicts to declare.

Data availability

The authors state that all data supporting the results of this study are provided in the article and its supplementary information (SI). Additional raw data are available from the corresponding author upon reasonable request. Supplementary information is available. See DOI: https://doi.org/10.1039/d5ta08305b.

Acknowledgements

This research was supported by the Hyundai Motor Company.

Notes and references

1 C.-Z. Zhao, P.-Y. Chen, R. Zhang, X. Chen, B.-Q. Li, X.-Q. Zhang, X.-B. Cheng and Q. Zhang, An ion redistributor for dendrite-free lithium metal anodes, *Sci. Adv.*, 2018, **4**, eaat3446.
2 J. B. Goodenough and Y. Kim, Challenges for rechargeable Li batteries, *Chem. Mater.*, 2010, **22**, 587–603.
3 M. Armand and J.-M. Tarascon, Building better batteries, *Nature*, 2008, **451**, 652–657.
4 J. W. Choi and D. Aurbach, Promise and reality of post-lithium-ion batteries with high energy densities, *Nat. Rev. Mater.*, 2016, **1**, 1–16.
5 X. Zhang, Y. Yang and Z. Zhou, Towards practical lithium-metal anodes, *Chem. Soc. Rev.*, 2020, **49**, 3040–3071.
6 M. He, L. G. Hector Jr, F. Dai, F. Xu, S. Kolluri, N. Hardin and M. Cai, Industry needs for practical lithium-metal battery designs in electric vehicles, *Nat. Energy*, 2024, **9**, 1199–1205.

7 S. Lee, K. Park, B. Koo, C. Park, M. Jang, H. Lee and H. Lee, Safe, stable cycling of lithium metal batteries with low-viscosity, fire-retardant locally concentrated ionic liquid electrolytes, *Adv. Funct. Mater.*, 2020, **30**, 2003132.
8 X. B. Cheng, R. Zhang, C. Z. Zhao and Q. Zhang, Toward Safe Lithium Metal Anode in Rechargeable Batteries: A Review, *Chem. Rev.*, 2017, **117**, 10403–10473.
9 R. Wang, W. Cui, F. Chu and F. Wu, Lithium metal anodes: Present and future, *J. Energy Chem.*, 2020, **48**, 145–159.
10 C. Fang, X. Wang and Y. S. Meng, Key issues hindering a practical lithium-metal anode, *Trends Chem.*, 2019, **1**, 152–158.
11 S. Li, M. Jiang, Y. Xie, H. Xu, J. Jia and J. Li, Developing High-Performance Lithium Metal Anode in Liquid Electrolytes: Challenges and Progress, *Adv. Mater.*, 2018, **30**, e1706375.
12 M. D. Tikekar, S. Choudhury, Z. Tu and L. A. Archer, Design principles for electrolytes and interfaces for stable lithium-metal batteries, *Nat. Energy*, 2016, **1**, 1–7.
13 M. Yeddala, L. Rynearson and B. L. Lucht, Modification of carbonate electrolytes for lithium metal electrodes, *ACS Energy Lett.*, 2023, **8**, 4782–4793.
14 J. Becking, A. Gröbmeyer, M. Kolek, U. Rodehorst, S. Schulze, M. Winter, P. Bieker and M. C. Stan, Lithium-metal foil surface modification: an effective method to improve the cycling performance of lithium-metal batteries, *Adv. Mater. Interfaces*, 2017, **4**, 1700166.
15 Y. Xie, Y. Huang, Y. Zhang, T. Wu, S. Liu, M. Sun, B. Lee, Z. Lin, H. Chen, P. Dai, Z. Huang, J. Yang, C. Shi, D. Wu, L. Huang, C. Wang and S. Sun, Surface modification using heptafluorobutyric acid to produce highly stable Li metal anodes, *Nat. Commun.*, 2023, **14**, 2883.
16 G. Lu, J. Nai, D. Luan, X. Tao and X. W. Lou, Surface engineering toward stable lithium metal anodes, *Sci. Adv.*, 2023, **9**, eadf1550.
17 R. Xu, X.-B. Cheng, C. Yan, X.-Q. Zhang, Y. Xiao, C.-Z. Zhao, J. Q. Huang and Q. Zhang, Artificial Interphases for Highly Stable Lithium Metal Anode, *Matter*, 2019, **1**, 317–344.
18 N. W. Li, Y. X. Yin, C. P. Yang and Y. G. Guo, An Artificial Solid Electrolyte Interphase Layer for Stable Lithium Metal Anodes, *Adv. Mater.*, 2016, **28**, 1853–1858.
19 M. S. Kim, J.-H. Ryu, Deepika, Y. R. Lim, I. W. Nah, K.-R. Lee, L. A. Archer and W. I. Cho, Langmuir–Blodgett artificial solid-electrolyte interphases for practical lithium metal batteries, *Nat. Energy*, 2018, **3**, 889–898.
20 G. H. Moon, H. J. Kim, I. S. Chae, S. C. Park, B. S. Kim, J. Jang, H. Kim and Y. S. Kang, An artificial solid interphase with polymers of intrinsic microporosity for highly stable Li metal anodes, *Chem. Commun.*, 2019, **55**, 6313–6316.
21 S. Wang, J. Zhang, L. Zhang, X. Li, R. Zhao, Y. Liu, Z. Wang, X. Lu, Y. Xin, H. Tian, F. Kang and B. Li, Revealing the synergistic effect of LiF and Li 3 N in solid electrolyte interphases for stable lithium metal batteries using in situ electrochemical atomic force microscopy, *J. Mater. Chem. A*, 2024, **12**, 5815–5823.
22 S. Wang, J. Zhang, L. Zhang, X. Hu, X. Qin, X. Yan, Z. Wang, X. Lu, Y. Xin, F. Kang, H. Tian and B. Li, 3D self-supporting core-shell silicon-carbon nanofibers-based host enables confined Li+ deposition for lithium metal battery, *Nano Energy*, 2024, **131**, 110255.
23 H. Tian, J. Zhang, B. He, Y. Liu, W. Li, F. Zhang, Z. Wang, X. Lu, Y. Xin and S. Wang, An artificial layer enables in situ generation of a homogeneous inorganic/organic composite solid electrolyte interphase for stable lithium metal batteries, *Nanoscale*, 2024, **16**, 18066–18075.
24 J.-M. Tarascon and M. Armand, Issues and challenges facing rechargeable lithium batteries, *Nature*, 2001, **414**, 359–367.
25 J. Song, G. Jeong, A.-J. Lee, J. H. Park, H. Kim and Y.-J. Kim, Dendrite-free polygonal sodium deposition with excellent interfacial stability in a NaAlCl4–2SO2 inorganic electrolyte, *ACS Appl. Mater. Interfaces*, 2015, **7**, 27206–27214.
26 B. R. Kim, G. Jeong, A. Kim, Y. Kim, M. G. Kim, H. Kim and Y. J. Kim, High Performance Na–CuCl2 Rechargeable Battery toward Room Temperature ZEBRA-Type Battery, *Adv. Energy Mater.*, 2016, **6**, 1600862.
27 K.-H. Kwak, H. J. Suh, A. Kim, S. Park, J. Song, S. Li, Y. Kim, G. Jeong, H. Kim and Y.-J. Kim, Reversible dual-ion battery via mesoporous Cu2O cathode in SO2-in-salt non-flammable electrolyte, *Nano Energy*, 2019, **66**, 104138.
28 A. Kim, H. Jung, J. Song, J. Lee, G. Jeong, Y. J. Kim and H. Kim, Self-Formulated Na-Based Dual-Ion Battery Using Nonflammable SO_2-Based Inorganic Liquid Electrolyte, *Small*, 2021, **17**, 1902144.
29 G. Jeong, H. Kim, J. H. Park, J. Jeon, X. Jin, J. Song, B.-R. Kim, M.-S. Park, J. M. Kim and Y.-J. Kim, Nanotechnology enabled rechargeable Li–SO 2 batteries: another approach towards post-lithium-ion battery systems, *Energy Environ. Sci.*, 2015, **8**, 3173–3180.
30 A. Kim, H. Jung, J. Song, H. J. Kim, G. Jeong and H. Kim, Lithium-ion intercalation into graphite in SO_2-based inorganic electrolyte toward high-rate-capable and safe lithium-ion batteries, *ACS Appl. Mater. Interfaces*, 2019, **11**, 9054–9061.
31 T. Gao, B. Wang, L. Wang, G. Liu, F. Wang, H. Luo and D. Wang, LiAlCl4· 3SO2 as a high conductive, non-flammable and inorganic non-aqueous liquid electrolyte for lithium ion batteries, *Electrochim. Acta*, 2018, **286**, 77–85.
32 U. Schily and J. Heitbaum, Reaction of clean lithium with O2, SO2 and liquid LiAlCl4· 3 (SO2), an XPS and Auger analysis, *Vacuum*, 1990, **41**, 1736–1738.
33 C. Yan, X.-B. Cheng, C.-Z. Zhao, J.-Q. Huang, S.-T. Yang and Q. Zhang, Lithium metal protection through in-situ formed solid electrolyte interphase in lithium-sulfur batteries: The role of polysulfides on lithium anode, *J. Power Sources*, 2016, **327**, 212–220.
34 K. Abraham and S. Chaudhri, The lithium surface film in the Li/SO 2 cell, *J. Electrochem. Soc.*, 1986, **133**, 1307.
35 G. Jeong, H. Kim, H. S. Lee, Y.-K. Han, J. H. Park, J. H. Jeon, J. Song, K. Lee, T. Yim, K. J. Kim, H. Lee, Y.-J. Kim and H.-J. Sohn, A room-temperature sodium rechargeable battery using an SO2-based nonflammable inorganic liquid catholyte, *Sci. Rep.*, 2015, **5**, 12827.
36 J. Lee, S. H. Choi, S. Do Mun, K. Kwak, S. Seo, K. H. Ryu and H. Kim, Fluorinated SO2-based inorganic electrolytes for

enhanced electrochemical performance in Li-metal anodes, *Chem. Eng. J.*, 2025, **509**, 161438.
37 T. Gao, B. Wang, J. Gao and D. Wang, Lithium fluoride additive for inorganic LiAlCl4· 3SO2 electrolyte toward stable lithium metal anode, *Electrochim. Acta*, 2020, **345**, 136193.
38 J. Zhang, S. Li, X. Wang, S. Mao, J. Guo, Z. Shen, J. Mao, Q. Wu, K. Shen, H. Cheng, Y. Tan and Y. Lu, Construction of Stable Li2O-Rich Solid Electrolyte Interphase for Practical PEO-Based Li-Metal Batteries, *Adv. Energy Mater.*, 2023, **14**, 2302587.
39 Z. Y. Wang, C. Z. Zhao, N. Yao, Y. Lu, Z. Q. Xue, X. Y. Huang, P. Xu, W. Z. Huang, Z. X. Wang and J. Q. Huang, The regulation of solid electrolyte interphase on composite lithium anodes in solid-state batteries, *Angew. Chem., Int. Ed.*, 2025, **64**, e202414524.
40 A. Li, W. Xin, Q. Wang, W. Ai, W. Han, C. Yang, Y. Wang, N. Du, C. Liu, Y. Zhang, X. Li and Y. Zhang, Study on an Interpenetrating Artificial SEI for Lithium Metal Anode Modification and Fast Charging Characterization, *ACS Appl. Mater. Interfaces*, 2024, **16**, 65984–65992.
41 H. Chen, A. Pei, D. Lin, J. Xie, A. Yang, J. Xu, K. Lin, J. Wang, H. Wang and F. Shi, Uniform high ionic conducting lithium sulfide protection layer for stable lithium metal anode, *Adv. Energy Mater.*, 2019, **9**, 1900858.
42 F. Liu, L. Wang, Z. Zhang, P. Shi, Y. Feng, Y. Yao, S. Ye, H. Wang, X. Wu and Y. Yu, A mixed lithium-ion conductive Li2S/Li2Se protection layer for stable lithium metal anode, *Adv. Funct. Mater.*, 2020, **30**, 2001607.
43 R. A. Huggins, Recent results on lithium ion conductors, *International Symposium on Solid Ionic and Ionic-Electronic Conductors*, 1977, pp. 773–781.
44 R. Guo and B. M. Gallant, Li2O solid electrolyte interphase: probing transport properties at the chemical potential of lithium, *Chem. Mater.*, 2020, **32**, 5525–5533.
45 J. S. Lowe and D. J. Siegel, Modeling the interface between lithium metal and its native oxide, *ACS Appl. Mater. Interfaces*, 2020, **12**, 46015–46026.
46 Y. Chen, C. Ouyang, L. Song and Z. Sun, Electrical and lithium ion dynamics in three main components of solid electrolyte interphase from density functional theory study, *J. Phys. Chem. C*, 2011, **115**, 7044–7049.
47 E. Nour, L. Chen and J. Laane, Far-infrared and Raman spectroscopic studies of polyiodides, *J. Phys. Chem.*, 1986, **90**, 2841–2846.
48 Y. Zhao, L. Wang and H. R. Byon, High-performance rechargeable lithium-iodine batteries using triiodide/iodide redox couples in an aqueous cathode, *Nat. Commun.*, 2013, **4**, 1896.
49 T. Shiga, Y. Kato, M. Inoue and Y. Hase, Bifunctional catalytic activity of iodine species for lithium–carbon dioxide battery, *ACS Sustain. Chem. Eng.*, 2019, **7**, 14280–14287.
50 H.-D. Lim, H. Park, H. Kim, J. Kim, B. Lee, Y. Bae, H. Gwon and K. Kang, A New Perspective on Li–SO2 Batteries for Rechargeable Systems, *Angew. Chem., Int. Ed.*, 2015, **54**, 9663–9667.
51 G. Chen, W. Li, X. Du, C. Wang, X. Qu, X. Gao, S. Dong, G. Cui and L. Chen, Transforming a primary Li-SOCl2 battery into a high-power rechargeable system via molecular catalysis, *J. Am. Chem. Soc.*, 2023, **145**, 22158–22167.
52 R. Magaa and J. Lannin, Observation of clustered molecules and ions in liquid iodine, *Phys. Rev. B: Condens. Matter Mater. Phys.*, 1985, **32**, 3819.
53 Y. Wang, Q. Sun, Q. Zhao, J. Cao and S. Ye, Rechargeable lithium/iodine battery with superior high-rate capability by using iodine–carbon composite as cathode, *Energy Environ. Sci.*, 2011, **4**, 3947–3950.
54 E. Lojou, R. Messina, J. Perichon, J. Descroix and G. Sarre, Electrochemical Study of Iodine in the LiAlCl4· 3 SO 2 Electrolyte, *J. Electrochem. Soc.*, 1989, **136**, 1270.
55 X. Li and X. Sun, Nitrogen-doped carbons in Li–S batteries: materials design and electrochemical mechanism, *Front. Energy Res.*, 2014, **2**, 49.
56 B. Zhong, J. Wu, L. Ren, T. Zhou, Z. Zhang, W. Liu and H. Zhou, Constructing a lithiophilic and mixed conductive interphase layer in electrolyte with dual-anion solvation sheath for stable lithium metal anode, *Energy Storage Mater.*, 2022, **50**, 792–801.
57 A. G. Wren, R. W. Phillips and L. U. Tolentino, Surface reactions of chlorine molecules and atoms with water and sulfuric acid at low temperatures, *J. Colloid Interface Sci.*, 1979, **70**, 544–557.
58 R. C. McDonald, W. P. Wang and S. Hankin, Coordination in thionyl chloride solutions of alkali metal salts, *J. Phys. Chem.*, 1992, **96**, 9760–9764.
59 P. H. Svensson and L. Kloo, Synthesis, structure, and bonding in polyiodide and metal iodide− iodine systems, *Chem. Rev.*, 2003, **103**, 1649–1684.
60 J. Wang, L. Li, H. Hu, H. Hu, Q. Guan, M. Huang, L. Jia, H. Adenusi, K. V. Tian, J. Zhang, S. Passerini and H. Lin, Toward dendrite-free metallic lithium anodes: from structural design to optimal electrochemical diffusion kinetics, *ACS Nano*, 2022, **16**, 17729–17760.
61 S. Liu, X. Ji, N. Piao, J. Chen, N. Eidson, J. Xu, P. Wang, L. Chen, J. Zhang, T. Deng, S. Hou, T. Jin, H. Wan, J. Li, J. Tu and C. Wang, An inorganic-rich solid electrolyte interphase for advanced lithium-metal batteries in carbonate electrolytes, *Angew. Chem., Int. Ed.*, 2021, **60**, 3661–3671.
62 C. Chen, Q. Liang, G. Wang, D. Liu and X. Xiong, Grain-boundary-rich artificial SEI layer for high-rate lithium metal anodes, *Adv. Funct. Mater.*, 2022, **32**, 2107249.
63 K. H. Chen, K. N. Wood, E. Kazyak, W. S. LePage, A. L. Davis, A. J. Sanchez and N. P. Dasgupta, Dead lithium: mass transport effects on voltage, capacity, and failure of lithium metal anodes, *J. Mater. Chem. A*, 2017, **5**, 11671–11681.
64 G. Yasin, M. Arif, T. Mehtab, X. Lu, D. Yu, N. Muhammad, M. T. Nazir and H. Song, Understanding and suppression strategies toward stable Li metal anode for safe lithium batteries, *Energy Storage Mater.*, 2020, **25**, 644–678.

65 Y. Li, J. Long, Y. Liang and J. Hu, Lithium dendrites puncturing separator induced galvanostatic charge/discharge test problem in Li-symmetric cells, *Ionics*, 2023, **29**, 4933–4938.

66 M. Rosso, C. Brissot, A. Teyssot, M. Dollé, L. Sannier, J. M. Tarascon, R. Bouchet and S. Lascaud, Dendrite short-circuit and fuse effect on Li/polymer/Li cells, *Electrochim. Acta*, 2006, **51**, 5334–5340.

67 D. Bedrov, O. Borodin and J. B. Hooper, Li+ transport and mechanical properties of model solid electrolyte interphases (SEI): insight from atomistic molecular dynamics simulations, *J. Phys. Chem. C*, 2017, **121**, 16098–16109.

68 P. Zhai, T. Wang, H. Jiang, J. Wan, Y. Wei, L. Wang, W. Liu, Q. Chen, W. Yang and Y. Cui, 3D artificial solid-electrolyte interphase for lithium metal anodes enabled by insulator–metal–insulator layered heterostructures, *Adv. Mater.*, 2021, **33**, 2006247.

69 G. Bieker, M. Winter and P. Bieker, Electrochemical in situ investigations of SEI and dendrite formation on the lithium metal anode, *Phys. Chem. Chem. Phys.*, 2015, **17**, 8670–8679.

70 Y. Liu, X. Xu, M. Sadd, O. O. Kapitanova, V. A. Krivchenko, J. Ban, J. Wang, X. Jiao, Z. Song, J. Song, S. Xiong and A. Matic, Insight into the critical role of exchange current density on electrodeposition behavior of lithium metal, *Adv. Sci.*, 2021, **8**, 2003301.

71 X.-X. Ma, X. Shen, X. Chen, Z.-H. Fu, N. Yao, R. Zhang and Q. Zhang, The origin of fast lithium-ion transport in the inorganic solid electrolyte interphase on lithium metal anodes, *Small Struct.*, 2022, **3**, 2200071.

72 X.-B. Cheng, C. Yan, H.-J. Peng, J.-Q. Huang, S.-T. Yang and Q. Zhang, Sulfurized solid electrolyte interphases with a rapid Li^+ diffusion on dendrite-free Li metal anodes, *Energy Storage Mater.*, 2018, **10**, 199–205.

73 W. Zhai, B. Yuan, Y. Fan, Y. Zhang, X. Zhang, Y. Ma, W. Liu and Y. Yu, Microstructure of lithium dendrites revealed by room-temperature electron microscopy, *J. Am. Chem. Soc.*, 2022, **144**, 4124–4132.

74 F. Kubel, B. Bertheville and H. Bill, Crystal structure of dilithiumsulfide, Li2S, *Z. Kristallogr.–New Cryst. Struct.*, 1997, **214**, 302.